



This is a repository copy of *Prenatal growth map of the mouse knee joint by means of deformable registration technique.*

White Rose Research Online URL for this paper:
<http://eprints.whiterose.ac.uk/140664/>

Version: Published Version

Article:

Giorgi, M. orcid.org/0000-0001-7763-8545, Sotiriou, V. orcid.org/0000-0003-2892-2915, Fanchini, N. et al. (4 more authors) (2019) Prenatal growth map of the mouse knee joint by means of deformable registration technique. PLoS One, 14 (1). e0197947. ISSN 1932-6203

<https://doi.org/10.1371/journal.pone.0197947>

Reuse

This article is distributed under the terms of the Creative Commons Attribution (CC BY) licence. This licence allows you to distribute, remix, tweak, and build upon the work, even commercially, as long as you credit the authors for the original work. More information and the full terms of the licence here:
<https://creativecommons.org/licenses/>

Takedown

If you consider content in White Rose Research Online to be in breach of UK law, please notify us by emailing eprints@whiterose.ac.uk including the URL of the record and the reason for the withdrawal request.



eprints@whiterose.ac.uk
<https://eprints.whiterose.ac.uk/>

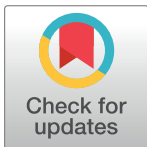
RESEARCH ARTICLE

Prenatal growth map of the mouse knee joint by means of deformable registration technique

Mario Giorgi^{1,2,3*}, Vivien Sotiriou⁴, Niccolo' Fanchini⁵, Simone Conigliaro⁵, Cristina Bignardi⁵, Niamh C. Nowlan⁴, Enrico Dall'Ara^{1,2}

1 Department of Oncology and Metabolism, University of Sheffield, Sheffield, United Kingdom, **2** INSIGNEO Institute for In Silico Medicine, University of Sheffield, Sheffield, United Kingdom, **3** Certara QSP, Certara UK Limited, Simcyp Division, Sheffield, United Kingdom, **4** Department of Bioengineering, Imperial College London, London, United Kingdom, **5** Department of Mechanics, Politecnico di Torino, Torino, Italy

* m.giorgi@sheffield.ac.uk



OPEN ACCESS

Citation: Giorgi M, Sotiriou V, Fanchini N, Conigliaro S, Bignardi C, Nowlan NC, et al. (2019) Prenatal growth map of the mouse knee joint by means of deformable registration technique. PLoS ONE 14(1): e0197947. <https://doi.org/10.1371/journal.pone.0197947>

Editor: María Angeles Pérez, Universidad de Zaragoza, SPAIN

Received: May 9, 2018

Accepted: December 9, 2018

Published: January 3, 2019

Copyright: © 2019 Giorgi et al. This is an open access article distributed under the terms of the [Creative Commons Attribution License](https://creativecommons.org/licenses/by/4.0/), which permits unrestricted use, distribution, and reproduction in any medium, provided the original author and source are credited.

Data Availability Statement: All data are available at <https://doi.org/10.15131/shef.data.7447406>.

Funding: The study was partially funded by the Engineering and Physical Sciences Research Council EP/K03877X/1 (<https://epsrc.ukri.org/>), and the European Research Council under the European Union's Seventh Framework Programme (ERC Grant agreement no. [336306]) (https://ec.europa.eu/research/fp7/index_en.cfm).

Competing interests: The authors of this manuscript have no affiliation with or involvement

Abstract

Joint morphogenesis is the process during which distinct and functional joint shapes emerge during pre- and post-natal joint development. In this study, a repeatable semi-automatic protocol capable of providing a 3D realistic developmental map of the prenatal mouse knee joint was designed by combining Optical Projection Tomography imaging (OPT) and a deformable registration algorithm (Sheffield Image Registration toolkit, SHIRT). Eleven left limbs of healthy murine embryos were scanned with OPT (voxel size: 14.63µm) at two different stages of development: Theiler stage (TS) 23 (approximately 14.5 embryonic days) and 24 (approximately 15.5 embryonic days). One TS23 limb was used to evaluate the precision of the displacement predictions for this specific case. The remaining limbs were then used to estimate Developmental Tibia and Femur Maps. Acceptable uncertainties of the displacement predictions computed from repeated images were found for both epiphyses (between 1.3µm and 1.4µm for the proximal tibia and between 0.7µm and 1.0µm for the femur, along all directions). The protocol was found to be reproducible with maximum Modified Hausdorff Distance (MHD) differences equal to 1.9 µm and 1.5 µm for the tibial and femoral epiphyses respectively. The effect of the initial shape of the rudiment affected the developmental maps with MHD of 21.7 µm and 21.9 µm for the tibial and femoral epiphyses respectively, which correspond to 1.4 and 1.5 times the voxel size. To conclude, this study proposes a repeatable semi-automatic protocol capable of providing mean 3D realistic developmental map of a developing rudiment allowing researchers to study how growth and adaptation are directed by biological and mechanobiological factors.

Introduction

Growth and morphogenesis are two fundamental processes which every living system undergo during both the prenatal and juvenile phase. If growth is more related to an increase in size and mass of an organism over a period of time, morphogenesis is the biological process, which

in any organization with any financial interest in the subject matter or material discussed in this manuscript. The Certara QSP, Certara UK Limited affiliation does not alter our adherence to PLOS ONE policies on sharing data and materials.

is responsible for any organism to develop its shape. Joint morphogenesis is the key process through which the two opposing cartilaginous rudiments of a joint develop their reciprocal and fully functional shapes, and which starts during prenatal joint development. This process is described in details by Pacifici et al., [1] and subsequently updated by Nowlan and Sharpe [2]. The consequences of incomplete or abnormal joint morphogenesis can be very debilitating and may lead to musculoskeletal diseases such as osteoarthritis (OA) [3, 4]. The formation of a skeletal joint is a highly regulated process which is controlled by several biochemical factors (e.g. growth factors, Hox genes) [5]. Moreover, several studies have experimentally found a relationship between prenatal joint motion and physiological joint morphogenesis in mice [6, 7] and chicks [8–11], demonstrating the importance of mechanical loads in the morphogenic process. For example, 2D histological assessment of chick embryos immobilised with neuromuscular blocking agents showed a reduction in width of the intercondylar fossa of the distal femur and of the proximal epiphysis of the tibiotarsus and fibula during knee joint morphogenesis [10], and up to 50% reduction in the epiphyseal width of the proximal and distal regions of the knee, tibiotarsus and metatarsus [9]. Despite the clinical relevance of morphogenesis, there is very little understanding about the factors driving this complex process [1]. Mechanobiological growth models have also been used to deepen our understanding on morphogenesis by exploring the role of motion or loading on joint shape [5, 12–15]. However, despite their undeniable importance these models have a series of limitations. For example, the 3D prenatal joint kinematics and kinetics are not measured accurately, and so far only generic loading conditions have been used for the Finite Element (FE) models. Moreover, idealized joint shapes were used instead of realistic shapes. Finally, due to a lack of information, the cascade of biochemical factors determining the amount of biological growth on which the mechanical stimuli operates were extremely simplified and considered to be proportional to the chondrocytes density in the region of interest [12, 13].

This study focuses on defining a methodology for better assessment of realistic shapes in the prenatal joint morphogenesis. Principal Component Analyses (PCA) [16, 17] is the gold standard method for the assessment of shape changes from medical images. However, this method is based on predefined modes of deformation and, due to the lack of large databases of prenatal rudiment shape changes, this approach could not be used for this application. The approach used in this study is based on deformable image registration [18, 19], which, due to the large number of degrees of freedom of the transformation, can feasibly be used to measure the heterogeneous variations of the developing rudiments.

In this study, we developed a repeatable semi-automatic protocol capable of providing a 3D realistic developmental map of the developing mouse knee joint by applying a deformable registration algorithm (Sheffield Image Registration toolkit, ShIRT [18–20]) to 3D images acquired *ex vivo* using Optical Projection Tomography (OPT) [21]. The robustness and repeatability of the protocol was evaluated with inter- and intra-operator tests. The developed protocol can be used to study the effect of mechanical and biological stimuli on the joint growth and morphogenesis, and to populate and validate computational models for prediction of joint development.

Materials and methods

Specimen preparation and imaging with Optical Projection Tomography

All samples were healthy embryos, either wildtype or heterozygous, for the Pax3 mutation from the Spd (Spotch delayed) strain. Pregnant females (source: Jax Laboratory) were humanely sacrificed by CO₂, cesarean section was performed during which the entire uterus was extracted. Embryos were separated from their membranes, decapitated and their forelimbs

and hindlimbs were dissected. Eleven limbs in total were used for this study, six of which were staged as Theiler Stage (TS23 [22] equivalent to approximately 14.5 embryonic days, and the remaining five which were staged as TS24 equivalent to approximately 15.5 embryonic days). One of the six TS23 embryos was scanned twice and the obtained images were registered to evaluate the precision of the deformable registration algorithm used to measure the developmental map [20]. The hindlimbs were stained with 0.015% Alcian Blue for cartilage [23] and processed for scanning with Optical Projection Tomography (OPT) [21] as reported in detail in [24]. OPT [25] constructs an image by measuring the amount of light transmitted or emitted by an object when light is shone upon it. A specimen is rotated 360 degrees and a series of 400 images in total were taken (rotation step equal to 0.9 degrees). The stack of images is then reconstructed using a back-projection algorithm (NRecon, Bruker microCT, Belgium), to compute a complete 3-D image of the specimen. The TS23 and TS24 hindlimbs used in this study were scanned with a 1.25 magnification (corresponding to a pixel size equal to 14.63 μm) and an exposure time ranging from 0.0008 sec^{-1} to 0.001 sec^{-1} . The size of each image was 490x590 pixels and the binning was set to 4x4. A source of white light was placed behind the rotating mount where the sample was mounted.

All procedures performed complied with the ethical European Legislation. The project license (No 7007442) used was approved by the Home Office and by the Governance Board for Animal Research at Imperial College London.

Elastic registration protocol

After image reconstruction of each scanned rudiment (NRecon, Bruker microCT, Belgium) the eleven distal femoral and the eleven proximal tibial epiphyses were cropped from the images of the hindlimbs by applying a single level threshold followed by a manual refinement of the initial segmentation based on visual checks in each orthogonal plane (AMIRA software 2017, Thermo Fisher Scientific). The two developmental stages used in this study (TS23 and TS24) were selected due to the fact that at earlier stages (<TS23) incomplete separation of the rudiments did not allow their proper identification, while at later stages (>T24), epiphyseal segmentation was compromised by advanced ossification in the diaphysis. Next, two of the TS23 images (a femoral epiphysis and a tibial epiphysis) were removed from the analysis and used to evaluate the precision of the deformable registration algorithm as described later in this section. A bounding box was then used to crop every remaining specimen by including a similar portion of the diaphysis (Fig 1A). The analyses were performed on the distal femur and on the proximal tibia to avoid the diaphysis, a region with limited or absent contrast in the OPT images due to the advanced ossification for the TS24 samples. In addition, one TS23 femoral epiphysis was excluded due to incomplete separation of the rudiments. All remaining TS23 tibial (N = 5) and femoral (N = 4) epiphyses were rigidly registered to each TS24 epiphyses through an automatic alignment of the centres of mass (AMIRA software function) followed by a manual adjustment of the orientation to align the main features of the rudiments (see Fig 1A and 1B). The effect of this operator-dependent step on the final outputs was evaluated with the inter- and intra-operator repeatability tests described later. A total of 25 and 20 rigid registrations were performed for the proximal tibia and the distal femur, respectively. The same bounding box was then used to resample all the images with a Lanczos interpolator [26]. To minimize the imperfections due to manual segmentation, a 3D erosion algorithm of 1 voxel was applied to all the images. Each pair of rigidly registered TS23-TS24 images was then registered with a deformable registration algorithm (ShIRT) [18, 20] in order to compute the displacements at the nodes of an isotropic grid superimposed to the images with nodal spacing (NS) equal to one voxel (14.63 μm). The procedure, reported in details elsewhere [20] is based

on the overlapping of the grid to the images to be registered, in the nodes of which the registration equations is solved. The approach includes an intensity displacement function, which allows changes in the grey levels between the two images. The displacements are interpolated with a tri-linear function between the nodes. The comparison metric is mutual information. ShIRT adds an additional smoothness constraint on the mapping optimized for each application. Moreover, the registration is performed starting from a large nodal spacing a few times smaller than the image size, until the chosen fine nodal spacing NS. In order to analyse only the results obtained for the rudiments, every cell of the grid with all nodes outside the TS23 binary image was removed by using a custom-made script (Matlab, The MathWorks, Inc.) [27].

The excluded TS23 sample was used to evaluate the uncertainties in the displacement predictions by registering two pairs of repeated scans of the whole prenatal femur and tibia following a procedure used for different bone structures [28, 29]. The precision of the method was evaluated for the three Cartesian directions using the standard deviation of the displacement components over the whole registration grid for tibia and femur. Uncertainties equal to 1.4 μm , 1.4 μm and 1.3 μm were found for the tibia along X, Y and Z directions, and uncertainties of 1.0 μm , 1.0 μm and 0.7 μm were found for the femur along X, Y and Z directions, respectively. These errors were considered acceptable for this application where displacements were at least one order of magnitude larger than the measured uncertainties.

Considering the absence of an *in vivo* longitudinal imaging modality for OPT measurements and the intrinsic variability of the shape of the rudiments at TS23 and TS24 (Fig 1A), the effect of including different input images on the final developmental map was estimated as follows (overview of the procedure in Fig 2).

In order to evaluate the effect of using different input images on the development maps for each anatomical location one randomly picked input image at TS23 was kept separate from the rest. Twenty displacement maps were generated by deformable registration of the remaining four three-dimensional images from the TS23 tibial epiphysis group with every three-dimensional image of the TS24 tibial epiphysis group. The obtained displacement values were averaged in order to generate a mean growth map (from now on referred to as “Developmental Tibia Map”, DTM). Furthermore, the average of five displacement maps obtained by registering the randomly picked image of the TS23 tibial epiphyses group with each one of the images in the TS24 tibial epiphysis group was computed in order to evaluate a control map (from now on referred to as “Single Tibia Map”, STM) (Fig 3A). The same procedure was then applied to

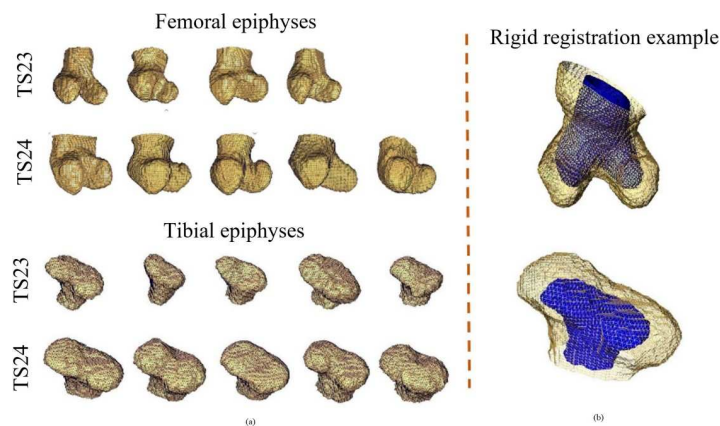


Fig 1. Reconstructed epiphyses used for the study and example of rigid registration. (a) femoral and tibial epiphyses (TS23 and TS24) used for the study; (b) example of rigidly registered femoral (top) and tibial (bottom) epiphyses. The TS23 epiphyses are represented in blue and the TS24 epiphyses in yellow.

<https://doi.org/10.1371/journal.pone.0197947.g001>

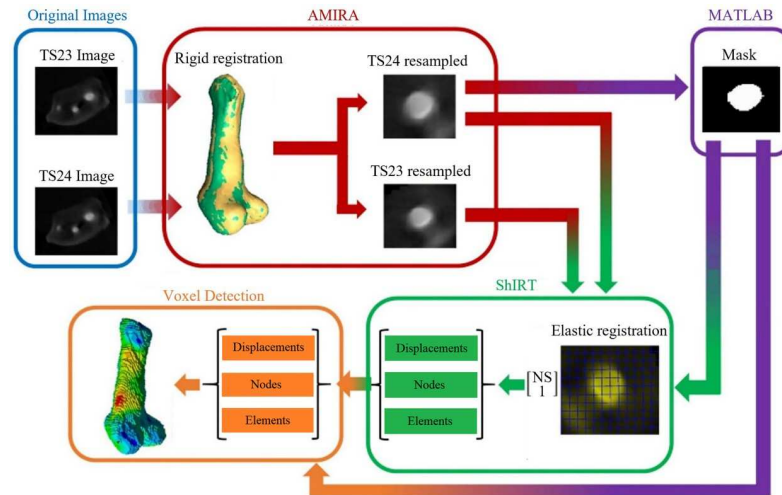


Fig 2. Methodological pipeline. Two OPT images at different developmental stages were acquired and rigidly registered. The new resampled images, together with a B/W image of the latest developmental stage (TS24) were then given as input to ShIRT. The calculated displacement were then filtered through the Voxel detection toolkit.

<https://doi.org/10.1371/journal.pone.0197947.g002>

the femur samples in order to generate the “Developmental Femur Map” (DFM), and “Single Femur Map” (SFM) (see Fig 3B).

For the visualization of the displacement maps for tibia and femur, the registration grids of the TS23 control specimens were converted into meshes of 8-node hexahedron elements, and

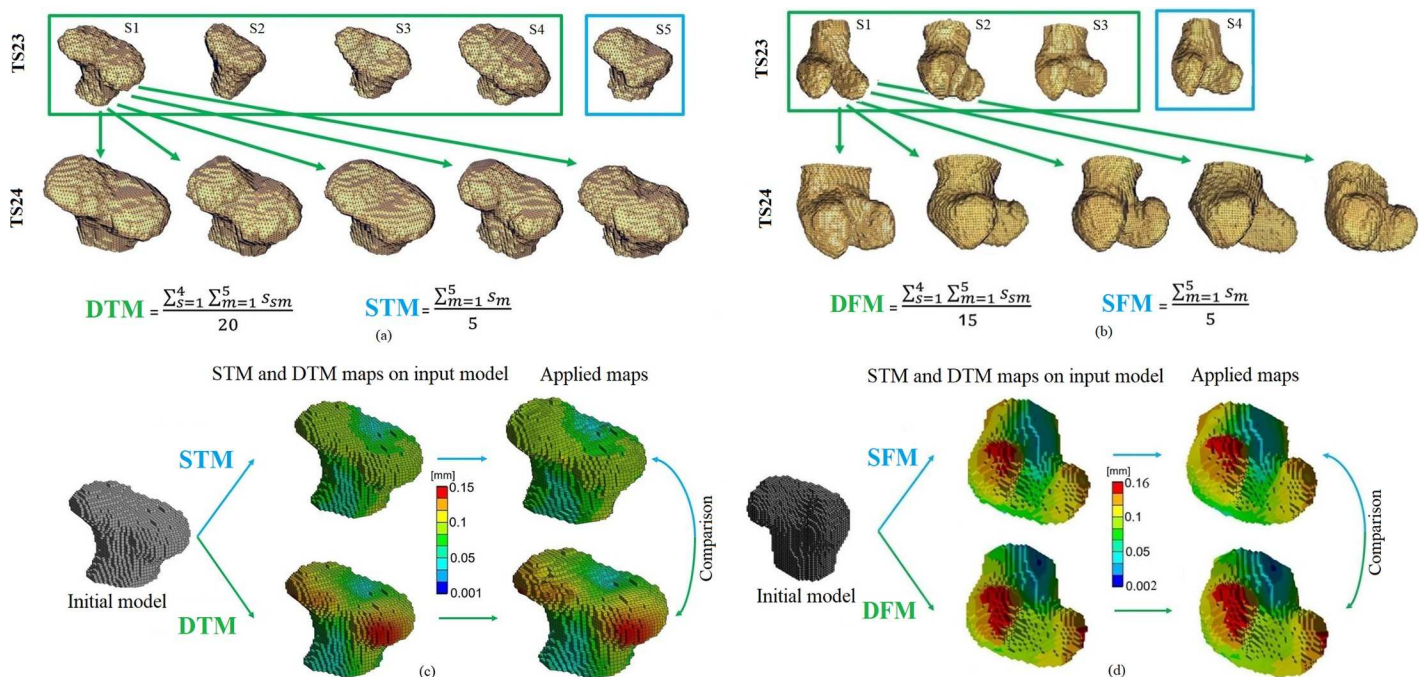


Fig 3. Schematic representation for the generation of both tibial and femoral maps. (a) Schematic representation of the twenty displacement maps (green box) and five displacement maps (blue box) generated by deformable registration for the tibia. The obtained maps were then averaged in order to generate a Developmental Tibia Map (DTM), and a Single Tibia Map (STM); (b) Schematic representation of the fifteen displacement maps (green box) and five displacement maps (blue box) generated by deformable registration for the femur. The obtained maps were then averaged in order to generate a Developmental Femur Map (DFM), and a Single Femur Map (SFM); (c) qualitative comparison between the DTM and the STM showing similar developmental patterns; (d) qualitative comparison between the DFM and the SFM showing similar developmental patterns.

<https://doi.org/10.1371/journal.pone.0197947.g003>

the “Developmental Maps” and “Single Maps” were applied as kinematic boundary conditions. A finite element (FE) software package (ANSYS, Mechanical APDL v.15.0, Ansys Inc, USA) was used to visualize and compare the maps (to be noted that no finite element analysis was performed and the FE package was used only for the visualization of the results).

Analyses and comparison of the growth maps

Two different analyses, briefly described below, were performed in this study: 1) Comparison of the Developmental and Single Maps for tibia (DTM, STM) and femur (DFM, SFM); 2) Evaluation of the protocol repeatability.

Comparison of the developmental and Single Maps for both anatomical sites. For both epiphyses, the displacement distributions of the Developmental Map and the Single Map were qualitatively compared after their application to the TS23 control FE mesh. Then, all the surface nodes of the new rudiment shapes were extracted using a custom-made script (Matlab, The MathWorks, Inc.), and their differences quantified using the Modified Hausdorff Distance (MHD) [30] and the Average Displacement Distance (ADD). The Hausdorff Distance (HD) is a metric used to measure the maximum and the minimum distances between all points of two given models. This metric can be used to determine the degree of resemblance between two superimposed objects [30]. Given two finite sets $A = \{a_1, \dots, a_p\}$ and $B = \{b_1, \dots, b_q\}$, the Hausdorff Distance is defined as:

$$HD(A, B) = \max(h(A, B), h(B, A))$$

Where

$$h(A, B) = \max_{a \in A} \min_{b \in B} \|a - b\|$$

The Modified Hausdorff Distance (MHD) it is a version of the HD which calculates the average of the minimum distances in order to remove possible errors due to outliers [31]. The Average Displacement Difference (ADD) consisted in calculating the average of all the displacement differences on each direction.

For visualization purposes, two STL surfaces were then generated by using the ball-pivoting technique [32] available in Meshlab.

Evaluation of the protocol repeatability. The repeatability of the protocol was evaluated through intra- (three repetitions) and inter-operator (one expert operator and two operators who followed guidelines) tests. For the tibial epiphyses, both tests were performed, while only the intra-operator test was performed on the femoral epiphyses. The part of the protocol mostly affected by operator decisions is the initial manual orientation of the rudiments. Therefore, the protocol was repeated from the initial upload of the raw images into Amira until the generation of the DTM, STM, DFM and SFM. The standard deviation of the MHD and ADD values for the three intra-operator repetitions and for the three inter-operator repetitions were computed.

Results

All data are available at <https://doi.org/10.15131/shef.data.7447406>.

Comparison of the developmental and Single Maps for both anatomical sites

A qualitative comparison between the Developmental Tibia and Femur Maps (DTM, DFM), and between the Single Tibia and Femur maps (STM, SFM) showed similar developmental

Table 1. Modified Hausdorff Distance (MHD) and Average Displacement Distance (ADD) values for all performed analyses for both tibial and femoral epiphyses. Values expressed in μm .

Tibial Epiphysis	MHD	MHD (range)	MHD (max difference)	ADD	ADD-X	ADD-Y	ADD-Z
Inter-Operator Test	20.0 \pm 0.2	19.8–20.2	0.4	28.8 \pm 0.2	28.6 \pm 0.5	31.9 \pm 0.6	25.8 \pm 0.3
Intra-Operator Test	21.1 \pm 0.3	22.2–22.4	0.4	29.9 \pm 0.8	30.0 \pm 2.2	33.7 \pm 1.6	28.5 \pm 1.0
Femoral Epiphysis	MHD	MHD (range)	MHD (max difference)	ADD	ADD-X	ADD-Y	ADD-Z
Intra-Operator Test	22.8 \pm 0.7	22.3–23.4	1.1	34.2 \pm 0.4	34.8 \pm 0.8	34.8 \pm 0.1	31.9 \pm 1.4

<https://doi.org/10.1371/journal.pone.0197947.t001>

patterns, with higher displacement values on the lateral and medial condyles of both rudiments compared to the inter-condylar region (Fig 3C and 3D). On a more quantitative aspect, displacements up to 150 μm and 100 μm were observed in the condyles region for the Developmental Tibia and Single Tibia maps respectively (DTM, STM), and displacements of approximately 60 μm were measured in the intercondylar region for both maps (Fig 3C). Similarly, displacements of up to 160 μm were observed in the condyles region for the Developmental Femur and Single Femur Maps (DFM, SFM) respectively, and displacements of approximately 80 μm were measured in the inter-condylar region for both maps (Fig 3D). When the effect of the initial shape of the rudiment over the developmental maps was quantified, MHD value of 21.7 μm and ADD values of 32.5 μm along X axis, of 35.6 μm along Y axis, and of 29.2 μm along Z axis were found between the Developmental Tibia Map (DTM) and the Single Tibia Map (STM) (Table 1).

When the same analysis was performed on the femoral epiphyses an MHD of 21.9 μm and an ADD of 34.2 μm , 34.9 μm , and 30.3 μm were found along X, Y, and Z axes respectively (Table 1). A qualitative comparison between the Developmental Tibia Map (DTM) and the Single Tibia Map (STM), and between Developmental Femur Map (DFM) and the Single Femur Map (SFM) is reported in Fig 4A.

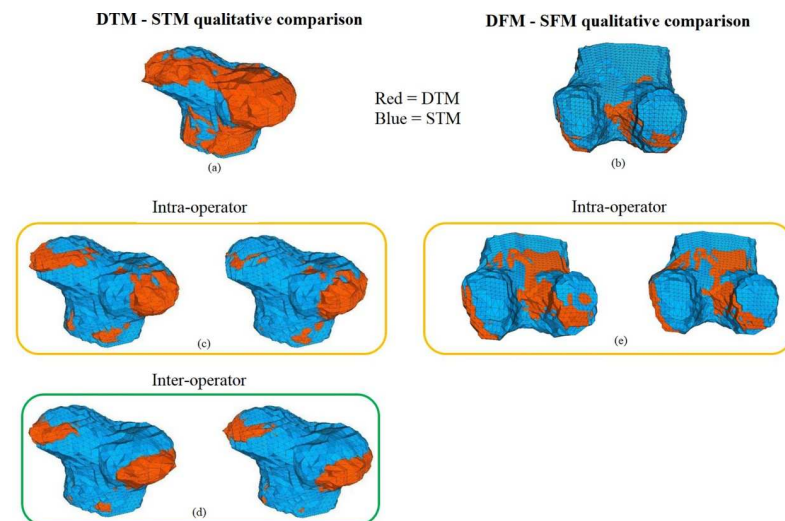


Fig 4. Qualitative comparison between maps. (a) Qualitative comparison between DTM (red) and STM (blue). (b) Qualitative comparison between DFM (red) and SFM (blue). (c) Qualitative comparison between the DTM (red) and STM (blue) for the two tibial femoral intra-operator tests. (d) Qualitative comparison between the DTM (red) and STM (blue) for the two tibial femoral inter-operator tests. (e) Qualitative comparison between the DFM (red) and SFM (blue) for the two tibial femoral intra-operator tests.

<https://doi.org/10.1371/journal.pone.0197947.g004>

Evaluation of the protocol repeatability

For the tibial epiphyses, MHD values of $22.1 \pm 0.4 \mu\text{m}$ and $20.0 \pm 0.3 \mu\text{m}$ were measured for the intra- and inter-operator test, respectively (see [Table 1](#)). A similar MHD intra-operator value was measured for the femoral rudiment ($22.5 \pm 0.8 \mu\text{m}$) (see [Table 1](#)). For intra-operator assessment of the tibial rudiment, ADD values of $30.0 \pm 2.2 \mu\text{m}$, $33.7 \pm 1.6 \mu\text{m}$, and $28.5 \pm 1.1 \mu\text{m}$ along X, Y, and Z axis respectively were calculated (see [Table 1](#)). Similar values were observed for the inter-operator test performed on the same rudiment with $28.6 \pm 0.6 \mu\text{m}$, $31.9 \pm 0.6 \mu\text{m}$, and $25.8 \pm 0.4 \mu\text{m}$ along X, Y, and Z axis, respectively (see [Table 1](#)). ADD values for the femoral rudiment, showed intra-operator values of $34.8 \pm 0.9 \mu\text{m}$, $34.8 \pm 0.1 \mu\text{m}$, and $31.9 \pm 1.4 \mu\text{m}$ along X, Y, and Z axis respectively (see [Table 1](#)). A qualitative comparison between intra- and inter-operator generated maps for both epiphyses is reported in [Fig 4C–4E](#).

Discussion

The aim of this study was to develop a repeatable semi-automatic protocol capable of providing a 3D realistic developmental map of the tibial and femoral developing rudiments in a prenatal mouse model. This was achieved by combining OPT imaging [[21](#)] and the deformable registration algorithm ShIRT [[18–20](#)].

The process of joint morphogenesis is key for physiological skeletal development. However, due to its complexity, there is very little understanding about the factors driving it [[1](#)]. Computational models have been used to deepen our understanding on the importance of fetal movement during development [[12–14](#)], but, these models are usually based on idealized shapes. The protocol developed in this study can be used to quantify the shape changes of a developing rudiment and provide 3D realistic displacement maps for studying the joint development, at different stages, in healthy or diseased animals and to populate computational models to study morphogenesis and its dependency on mechanical and biological stimuli. Indeed, by applying the presented approach to paralyzed mice (assuming that development under flaccid paralysis reduce to a minimum the influence of mechanical stimuli) we could understand independently the influence of both mechanical and biological stimuli during development. The protocol was found to be strongly reproducible for both epiphyses, with small intra- (SD of ADD below $2.2 \mu\text{m}$ for tibia and $1.4 \mu\text{m}$ for femur) and inter-operator (SD of ADD below $0.6 \mu\text{m}$ for tibia) displacement uncertainties ([Table 1](#)). The high reproducibility of this protocol enables researchers not familiar with elastic registration to generate reliable developmental maps. In addition, the maximum reproducibility error measured in terms of ADD ($2.2 \mu\text{m}$) suggests that this method is suitable to study all deformations of at least one order of magnitude higher (all deformations higher than $22 \mu\text{m}$) and this method could be used in the future to generate growth maps for earlier stages where the experimentally observed deformations have not yet been quantified precisely. The robustness of the method is also highlighted by the similarity between the reproducibility errors for the two anatomical rudiments and among the Cartesian directions.

For the developmental stages analyzed (TS23 and TS24), the generated maps for both anatomical sites showed higher growth corresponding to the condyle regions and lower growth in the intercondylar fossa. In addition, the DTM and the DFM showed mean displacement values of $75 \mu\text{m}$ and $81 \mu\text{m}$, with maxima values of $150 \mu\text{m}$ and $160 \mu\text{m}$ for the tibia and femur respectively ([Fig 3C and 3D](#)). When the DTM and DFM were qualitatively compared with the STM and SFM, the analyses showed, as expected, similar but not identical developmental patterns ([Fig 3C and 3D](#)). Maximum MHD between the measured displacement maps of $21 \mu\text{m}$ and $22 \mu\text{m}$ were found for the tibial and femoral maps, showing the variability of the growth among specimens. This value, ten times higher than the estimated uncertainties, underlines

the important role that the input images play. In fact, the high variability in the developmental maps found in this study is probably based on the differences in shape found especially at TS23 for both tibial and femoral rudiments (see Fig 1 for examples). Such variability could be probably reduced by increasing the sample size, to account for intrinsic differences among the specimens, or by extending the OPT imaging to *in vivo* application. However, this is not possible right now due to the necessity of culling the animal for staining the embryonic tissue to achieve enough contrast in the images.

This study has a few limitations. Firstly, the analyses were performed on the distal femur and on the proximal tibia only due to the limited or absent contrast in the OPT images due to the advanced diaphysis ossification for the TS24 samples. A combination between OPT and micro-CT (micro-computer tomography) imaging could help to overcome this problem and allow the application of this protocol to the whole rudiments. Secondly, a more comprehensive developmental map including earlier and later developmental stages could not be generated. The former because at earlier developmental stages the joints were not fully cavitated, making very difficult the identification of specific joint segments. The latter due to the advanced ossification process, which started involving the epiphyses. Finally, the analysis was performed on only 4 or 5 specimens per group. As the final goal is to create a mean biological growth map, including more specimens (and therefore more registrations) would reduce the influence of the differences in initial shape of the joints at the two TS and of the uncertainties of the procedure.

In conclusion, in this study we have shown how a combination of OPT imaging and deformable registration can be used to generate 3D realistic transformations of a developing rudiment in the prenatal mouse knee joint. The method is highly reproducible and will allow us to study how growth and adaptation are directed by biological and mechanobiological factors. Moreover, the realistic shapes can be used to generate more accurate computational models capable of exploring the influence of both physiological and non-physiological mechanical conditions on the process of morphogenesis and joint development.

Acknowledgments

The authors gratefully acknowledge Dr. Gareth Fletcher for implementing the DVC service, Sara Oliviero and Maria Cristiana Costa for helping with the repeatability tests.

Author Contributions

Conceptualization: Mario Giorgi.

Data curation: Mario Giorgi, Vivien Sotiriou.

Formal analysis: Mario Giorgi, Niccolo' Fanchini, Simone Conigliaro.

Funding acquisition: Enrico Dall'Ara.

Investigation: Mario Giorgi.

Methodology: Mario Giorgi.

Project administration: Mario Giorgi.

Resources: Cristina Bignardi, Niamh C. Nowlan.

Supervision: Mario Giorgi, Enrico Dall'Ara.

Writing – original draft: Mario Giorgi.

Writing – review & editing: Mario Giorgi, Niamh C. Nowlan, Enrico Dall'Ara.

References

1. Pacifici M, Koyama E, Iwamoto M. Mechanisms of synovial joint and articular cartilage formation: Recent advances, but many lingering mysteries. *Birth Defects Research Part C: Embryo Today: Reviews*. 2005; 75(3):237–48. <https://doi.org/10.1002/bdrc.20050> PMID: 16187328
2. Nowlan NC, Sharpe J. Joint shape morphogenesis precedes cavitation of the developing hip joint. *Journal of Anatomy*. 2014; 224(4):482–9. <https://doi.org/10.1111/joa.12143> PubMed PMID: PMC4098681. PMID: 24266523
3. Hogervorst T, Eilander W, Fikkers JT, Meulenbelt I. Hip ontogenesis: how evolution, genes, and load history shape hip morphotype and cartilotype. *Clinical orthopaedics and related research*. 2012; 470(12):3284–96. Epub 2012/08/29. <https://doi.org/10.1007/s11999-012-2511-4> PMID: 22926490; PubMed Central PMCID: PMC3492609.
4. Sandell LJ. Etiology of osteoarthritis: genetics and synovial joint development. *Nature Reviews Rheumatology*. 2012; 8:77. <https://doi.org/10.1038/nrrheum.2011.199> PMID: 22231237
5. Comellas E, Carriero A, Giorgi M, Pereira A, Shefelbine SJ. Chapter 2—Modeling the Influence of Mechanics on Biological Growth. *Numerical Methods and Advanced Simulation in Biomechanics and Biological Processes*: Academic Press; 2018. p. 17–35.
6. Nowlan NC, Bourdon C, Dumas G, Tajbakhsh S, Prendergast PJ, Murphy P. Developing bones are differentially affected by compromised skeletal muscle formation. *Bone*. 2010; 46(5):1275–85. Epub 2009/12/02. <https://doi.org/10.1016/j.bone.2009.11.026> PMID: 19948261; PubMed Central PMCID: PMC3492609.
7. Kahn J, Shwartz Y, Blitz E, Krief S, Sharir A, Breitel DA, et al. Muscle contraction is necessary to maintain joint progenitor cell fate. *Developmental cell*. 2009; 16(5):734–43. Epub 2009/05/23. <https://doi.org/10.1016/j.devcel.2009.04.013> PMID: 19460349.
8. Mikic B, Wong M, Chiquet M, Hunziker EB. Mechanical modulation of tenascin-C and collagen-XII expression during avian synovial joint formation. *Journal of Orthopaedic Research*. 2000; 18(3):406–15. <https://doi.org/10.1002/jor.1100180312> PMID: 10937627
9. Osborne AC, Lamb KJ, Lewthwaite JC, Dowthwaite GP, Pitsillides AA. Short-term rigid and flaccid paralysis diminish growth of embryonic chick limbs and abrogate joint cavity formation but differentially preserve pre-cavitated joints. *Journal of musculoskeletal & neuronal interactions*. 2002; 2(5):448–56. Epub 2005/03/11. PMID: 15758413.
10. Roddy KA, Prendergast PJ, Murphy P. Mechanical Influences on Morphogenesis of the Knee Joint Revealed through Morphological, Molecular and Computational Analysis of Immobilised Embryos. *PLOS ONE*. 2011; 6(2):e17526. <https://doi.org/10.1371/journal.pone.0017526> PMID: 21386908
11. Nowlan NC, Chandaria V, Sharpe J. Immobilized chicks as a model system for early-onset developmental dysplasia of the hip. *Journal of Orthopaedic Research*. 2014; 32(6):777–85. <https://doi.org/10.1002/jor.22606> PMID: 24590854
12. Heegaard JH, Beaupré GS, Carter DR. Mechanically modulated cartilage growth may regulate joint surface morphogenesis. *Journal of Orthopaedic Research*. 1999; 17(4):509–17. <https://doi.org/10.1002/jor.1100170408> PMID: 10459756
13. Giorgi M, Carriero A, Shefelbine SJ, Nowlan NC. Mechanobiological simulations of prenatal joint morphogenesis. *Journal of biomechanics*. 2014; 47(5):989–95. <https://doi.org/10.1016/j.jbiomech.2014.01.002> PMID: 24529755
14. Giorgi M, Carriero A, Shefelbine SJ, Nowlan NC. Effects of normal and abnormal loading conditions on morphogenesis of the prenatal hip joint: application to hip dysplasia. *Journal of biomechanics*. 2015; 48(12):3390–7. <https://doi.org/10.1016/j.jbiomech.2015.06.002> PMID: 26163754
15. Giorgi M, Verbruggen SW, Lacroix D. In silico bone mechanobiology: modeling a multifaceted biological system. *Wiley interdisciplinary reviews Systems biology and medicine*. 2016; 8(6):485–505. Epub 2016/09/08. <https://doi.org/10.1002/wsbm.1356> PMID: 27600060; PubMed Central PMCID: PMC3492609.
16. Galea GL, Hannuna S, Meakin LB, Delisser PJ, Lanyon LE, Price JS. Quantification of Alterations in Cortical Bone Geometry Using Site Specificity Software in Mouse models of Aging and the Responses to Ovariectomy and Altered Loading. *Frontiers in Endocrinology*. 2015; 6:52. <https://doi.org/10.3389/fendo.2015.00052> PubMed PMID: PMC4407614. PMID: 25954246
17. Varzi D, Coupaud SAF, Purcell M, Allan DB, Gregory JS, Barr RJ. Bone morphology of the femur and tibia captured by statistical shape modelling predicts rapid bone loss in acute spinal cord injury patients. *Bone*. 2015; 81(Supplement C):495–501. <https://doi.org/10.1016/j.bone.2015.08.026>
18. Barber D, Hose D. Automatic segmentation of medical images using image registration: diagnostic and simulation applications. *Journal of medical engineering & technology*. 2005; 29(2):53–63.

19. Barber DC, Oubel E, Frangi AF, Hose D. Efficient computational fluid dynamics mesh generation by image registration. *Medical image analysis*. 2007; 11(6):648–62. <https://doi.org/10.1016/j.media.2007.06.011> PMID: [17702641](https://pubmed.ncbi.nlm.nih.gov/17702641/)
20. Dall'Ara E, Barber D, Viceconti M. About the inevitable compromise between spatial resolution and accuracy of strain measurement for bone tissue: A 3D zero-strain study. *Journal of biomechanics*. 2014; 47(12):2956–63. <https://doi.org/10.1016/j.jbiomech.2014.07.019> PMID: [25113806](https://pubmed.ncbi.nlm.nih.gov/25113806/)
21. Sharpe J. Optical Projection Tomography. *Annual Review of Biomedical Engineering*. 2004; 6(1):209–28. <https://doi.org/10.1146/annurev.bioeng.6.040803.140210> PMID: [15255768](https://pubmed.ncbi.nlm.nih.gov/15255768/).
22. Theiler K. *The house mouse. Development and normal stages from fertilization to 4 weeks of age*. Berlin/Heidelberg, New York, Springer-Verlag.1972. 168 pp. p.
23. Johnson M. *Manipulating the mouse embryo: A laboratory manual*: by B. Hogan, F. Constantini and E. Lacy, Cold Spring Harbor Laboratory, 1986. \$60.00 (332 pages) ISBN 0 87969 175 1. *Trends in Genetics*. 1986; 2:298. [https://doi.org/10.1016/0168-9525\(86\)90275-1](https://doi.org/10.1016/0168-9525(86)90275-1).
24. Quintana L, Sharpe J. Preparation of mouse embryos for optical projection tomography imaging. *Cold Spring Harbor protocols*. 2011; 2011(6):664–9. Epub 2011/06/03. <https://doi.org/10.1101/pdb.prot5639> PMID: [21632773](https://pubmed.ncbi.nlm.nih.gov/21632773/).
25. Sharpe J, Ahlgren U, Perry P, Hill B, Ross A, Hecksher-Sorensen J, et al. Optical projection tomography as a tool for 3D microscopy and gene expression studies. *Science* (New York, NY). 2002; 296(5567):541–5. Epub 2002/04/20. <https://doi.org/10.1126/science.1068206> PMID: [11964482](https://pubmed.ncbi.nlm.nih.gov/11964482/).
26. Turkowski K. Filters for common resampling tasks. In: Andrew SG, editor. *Graphics gems*: Academic Press Professional, Inc.; 1990. p. 147–65.
27. Giorgi M, Dall'Ara E. Variability in strain distribution in the mice tibia loading model: A preliminary study using digital volume correlation. *Medical Engineering and Physics*. <https://doi.org/10.1016/j.medengphy.2018.09.001> PMID: [30243888](https://pubmed.ncbi.nlm.nih.gov/30243888/)
28. Dall'Ara E, Peña-Fernández M, Palanca M, Giorgi M, Cristofolini L, Tozzi G. Precision of Digital Volume Correlation Approaches for Strain Analysis in Bone Imaged with Micro-Computed Tomography at Different Dimensional Levels. *Frontiers in Materials*. 2017; 4(31). <https://doi.org/10.3389/fmats.2017.00031>
29. Palanca M, Bodey AJ, Giorgi M, Viceconti M, Lacroix D, Cristofolini L, et al. Local displacement and strain uncertainties in different bone types by digital volume correlation of synchrotron microtomograms. *Journal of biomechanics*. 2017; 58:27–36. Epub 2017/05/02. <https://doi.org/10.1016/j.jbiomech.2017.04.007> PMID: [28457604](https://pubmed.ncbi.nlm.nih.gov/28457604/).
30. Huttenlocher DP, Klanderman GA, Rucklidge WJ. Comparing images using the Hausdorff distance. *IEEE Transactions on Pattern Analysis and Machine Intelligence*. 1993; 15(9):850–63. <https://doi.org/10.1109/34.232073>
31. Dubuisson M, Jain AK, editors. A modified Hausdorff distance for object matching. *Proceedings of 12th International Conference on Pattern Recognition*; 1994 9–13 Oct. 1994.
32. Bernardini F, Mittleman J, Rushmeier H, Cl, #225, Silva u, et al. The Ball-Pivoting Algorithm for Surface Reconstruction. *IEEE Transactions on Visualization and Computer Graphics*. 1999; 5(4):349–59. <https://doi.org/10.1109/2945.817351>